

Fabrication of porous stainless steel pellets for physical modeling of supercritical extraction

By Manuela Covaciu, Eduardo Richter, Magdalena Walczak, Jin-Chong Tan and José M. del Valle*

[*] *Magdalena Walczak, Manuela Covaciu*

Department of Mechanical and Metallurgical Engineering

Pontificia Universidad Católica (UC) de Chile

Avda. Vicuña Mackenna 4860, Macul, Santiago, (Chile)

E-mail: mwalczak@ing.puc.cl

Jin-Chong Tan, Manuela Covaciu

Multifunctional Materials and Composites (MMC) Laboratory, Department of Engineering Science, University of Oxford, Parks Road, Oxford OX1 3PJ, UK

José M. del Valle, Eduardo Richter

Department of Chemical and Bioprocess Engineering

Pontificia Universidad Católica (UC) de Chile

[**] *This research has been supported by Fondo Nacional de Desarrollo Científico y Tecnológico Chile (FONDECYT), project N°3120186 and project N°1120827.*

Abstract

In this paper, a method of fabricating metallic analogues of biological materials is presented. In particular, the structure of pre-pressed oilseed used for physical modeling of supercritical CO₂ extraction of desired substances is replicated in a material commonly used for manipulation of foods, i.e. food grade stainless steel (AISI 316L).

Powder metallurgy approach is employed through sintering the steel powder with SiO₂ spacer and further leaching the porogen. The resulting metal framework has interconnected porosity and low apparent density (about 1.91 g/cm³). The prospect of tuning the balance between porosity and interconnectivity of pores is of special concern to allow mimicking the structure of natural materials intended for supercritical CO₂ extraction. With this motivation, the effects of initial silica content (between 20 to 60 vol.%) and silica particle size (small: 0.5-10 µm, medium: 110 µm, and large: 170-630 µm) on the structural and mechanical properties of the porous material are studied. It is found that increasing porosity correlates with decreasing compressive strength, whereas the plateau region of the stress-strain relationship in compression is of lower slope and spans over larger strain. Yield strength ranges from 4.2 MPa to 220 MPa, which is sufficient for sustaining the conditions of supercritical extraction.

1. Introduction

Supercritical carbon dioxide (CO₂) is an attractive alternative to the conventional liquid solvents for the extraction of desirable compounds (*e.g.*, bitter and aromatic compounds from hop for the beer), or the removal of undesirable contaminants (*e.g.*, caffeine and other alkaloids from coffee grains) from biological substrates.^[1] A supercritical fluid (or dense gas) is a substance that is at state conditions above its corresponding critical temperature (30.9°C for CO₂^[2]) and critical pressure (73.8 bar for CO₂^[2]). Under supercritical conditions, molecules form clusters of high local density (the same as in liquid state) that barely interact with each other (the same as in gas state) providing respectively solvation power and excellent transport properties (low viscosity, high self-diffusivity) to supercritical fluids.^[1] The near-liquid density allows dissolution of target solutes from complex matrices, whereas the near-gas transport properties allows fast extractions. Furthermore –unlike conventional liquid solvents– the physical properties of supercritical fluids can be tuned to specific

extraction needs by changing the state conditions making them highly selective as solvents.^[1] Finally, being CO₂ a gas under normal conditions, completely removing it from the extract and treated matrix to minimize contamination is an easy task (unlike liquid solvents).

Despite its advantages, large-scale industrial implementation of supercritical CO₂ extraction of solid substrate particles in packed beds has been limited by the necessity of predicting cumulative extraction curves of the desired compound(s) (or extract) as a function of extraction conditions, vessel size, and plant layout.^[3] This cumulative extraction curve is a complex function of kinetic parameters describing internal and external resistances to mass transfer (*i.e.*, within the substrate particles and between the particle surface and CO₂, respectively), and phase equilibrium parameters. Equilibrium factors can be measured independently.^[4,5] External resistance to mass transfer can be estimated using dimensionless correlations for mass transfer in packed beds operating with supercritical fluids.^[6] Finally, internal resistance to mass transfer depends on the effective diffusivity of the extract in the solid matrix or an alternative mass transfer coefficient that is generally fitted to cumulative extraction curves experimentally measured using an appropriate mass transfer model.^[6]

In order to determine the relationship between the inner structure of the substrate and the microstructural mass transfer factor experiments with model materials can be conducted. Vegetable substrates are pretreated prior to supercritical CO₂ extraction to speed up the extraction process, which typically includes particle size reduction to rupture mass transfer barriers such as cell walls, and to shorten diffusion paths. A vegetable substrate can be sheared *e.g.*, by flaking, prepressing, or pelletizing (which also causes cell wall rupture without relying in particle size reduction and undesirable production of fines).^[7-9] Microstructurally, these sheared substrates can be viewed as an interconnected pore network containing condensed extract that is removed by a diffusional^[7,8] or shrinking core^[3,9] mechanism: inner mass transfer can be characterized by a single, particle-size and CO₂-condition-independent microstructural mass transfer factor (the ratio between extract diffusivity in the solid matrix, and the binary diffusion coefficient of the extract in CO₂) that can be best-fitted to laboratory extractions.^[3,7-9] Having a material of well-known properties simplifies the subsequent modeling. Stüber et al.^[10] employed porous cylinders of bronze to model internal mass transfer of liquid solutes and to calculate the mass transfer coefficients. However, for edible compounds, the model material besides of mimicking the original structure of the biological matrix must necessarily be of food grade, (*i.e.*, do not alter foodstuff or contaminate it with harmful compounds).

In this paper, we present a method of fabricating a model structure of a pre-pressed oil seed, used for instance for the extraction of specialty vegetable oils, in a material commonly used for manipulation of foods, i.e. food grade AISI 316L stainless steel. The process of manufacturing porous steel belongs to the field of cellular materials, also referred to as metal foams, and has caught attention in the past decades due to the possibility of combining bulk metal properties, such as high strength, with high porosity that enables lightweight design^[11]. However, a valid difficulty in fabrication of cellular metals is the control and limitation of the achievable porous structure (percentage of volume, open vs. closed porosity, pore shape, pore size and size distribution) posing a challenge when a particular structure is to be replicated.

The technology for production of cellular metals methods is highly specific to the alloy system with Al-alloys being the most explored^[12] due to its relatively low melting point permitting direct foaming of hydrides.^[13] The classical techniques to produce porous metals are not applicable to steel and the available alternatives include the use of oxide or polymer foaming precursor, metal powder or fiber network sintering^[14], molding with a removable space holder.^[15]

Sintering of metal powders is used to produce a maximum of 30% porosity;^[16] the porosity can be increased by low compaction pressures of the powder metal (PM) or reduced sintering time in order to avoid densification during the heat treatment stage. The porosity can be increased even higher by adding a space holder to the metal powder during the mixing stage, followed by compaction and sintering of the PM. The high porosity is obtained when the space holder is removed^[17]. The method permits a very good control on overall porosity, pore size, and pore shape. Studies reported on this production method for porous steel use as space holder carbamide (removed by water leaching)^{[18]–[20]}, polymers (removed by evaporation)^[21] or SiC (removed with hydrofluoric acid)^[22]. The metal powder space-holder (MPSH) method is also used to produce porous steel without compression: polymer sponge space holder is infiltrated with metal powder under suspension followed by burning of the polymer at low temperature and followed by pressureless sintering of metal powder.^[23]

To the best of our knowledge, none of the reported MPSH techniques^{[14], [19], [21], [24]} produces porous steel using silica as the space holder. In this paper we present the possibilities and discuss the limitations of the method employed for fabricating porous AISI 316L. A special concern is the prospect of tuning the balance between porosity and interconnectivity that is necessary for mimicking the structure of pre-pressed oil seed intended for the supercritical CO₂ extraction of compounds.

2. Experimental

2.1. Fabrication of porous stainless steel

The model material was fabricated in the form of cylinders of 8 mm diameter and 10 mm height. The cylinders were obtained through the MPSH technique, compacting AISI 316L stainless steel with silica powder of differing particle size distributions: particles of 0.5-10 μm further referred to as small (S), particles <110 μm further referred to as medium (M), and particles of 170-630 μm further referred to large (L). The powders were acquired from Sigma-Aldrich and their specifications are summarized along with other fabrication parameters in **Table 1**. The mixtures were compacted in a cylindrical die employing axial pressure of 400 MPa, followed by sintering at 1200°C under H_2 atmosphere for 1 h. The mixing, compacting, and sintering was carried out by GKN Sinter Metals GmbH.

Samples that had retained sufficient handling strength after sintering were further subjected to removal of the silica spacer by leaching in 1 M NaOH at 60°C until stagnation in the cumulative mass loss. The last process as a function of leaching took from 12 days for samples L and 17 days for samples M. The amount of silica removed in time is shown in **Fig. 1**, in terms of both the mass fraction of the initially entrapped silica as well as the real density, ρ_{real} , which was calculated using **Eq. 1**:

$$\rho_{\text{real}} = \frac{m}{V_{\text{real}}} = \frac{m}{V_{316\text{L}} + V_{\text{SiO}_2}}, \quad (1)$$

where m , V_{real} , $V_{316\text{L}}$, and V_{SiO_2} are mass determined by weighing the sample, real volume of the final sample determined by N_2 -pycnometry (Ultracyc 1200e, Quantachrome®, Boynton Beach, FL), volume of the steel fraction determined from the initial condition, and volume of the SiO_2 fraction that diminishes during leaching, respectively. The resulting porous materials were then dried at 105°C to remove the rests of the solvents and analyzed.

2.2 Materials Characterization

Characterization studies included both structural analysis and determination of mechanical properties. Visual inspection of samples after sintering and after leaching was conducted to assess the handling strength. Samples that did not experience visual change when manually manipulated with hand were assigned “good” handling strength, whereas samples that would experience little crumbling were assigned “poor” handling strength, and samples that disintegrated during processing were classified as not acceptable and marked with “-” in

Table 1. For evaluation of microstructure, axial and radial cross-sections were prepared using a low-speed diamond saw (Buehler Isomet). Surface of the sections were grinded with sand papers of consecutive grits 40, 80, 150, 280, 1000 and 2000, followed by polishing with 3, 1 and 0.25 μm diamond polishing suspensions. In order to prevent the loss of silica in the process, vibrations during the cutting, grinding, and polishing were avoided.

Table 1. Sample specifications and qualitative analysis of the fabrication process.

Sample	SiO ₂ filler ^a	Filler vol.% ^b	Compaction quality	Sintering quality	Handling strength	Porosity %	Density, ρ [g·cm ⁻³]	Bulk density, ρ_{real} [g·cm ⁻³]
R-0	-	0	Good	Good	Good	25	5.94	7.74
S-30	S5631	30	Bad filling	Few cracks	-	43	4.39	7.33
S-40	S5631	40	Bad filling/cracks	Cracks	-	47	3.56	7.11
S-50	S5631	50	Bad filling/not compact	-	-	-	-	-
S-60	S5631	60	Cracks/not compact	-	-	-	-	-
M-20	83340	20	Good	Good	-	29	4.97	6.94
M-40	83340	40	Good	Few cracks	-	43	4.03	6.13
M-60	83340	60	Good	Cracks	-	-	-	-
L-20	84878	20	Good	Good	Good	45	4.12	7.84
L-40	84878	40	Few cracks	Few cracks	Good	63	2.68	7.83
L-60	84878	60	Few cracks	Heavy cracks	Poor	72	1.91	7.71

[a] SKU by Sigma-Aldrich [b] Filler vol.% in the compacted samples before sintering

Metallographic evaluation was carried out using an optical microscope Nikon Optiphot-100 with an integrated digital camera Moticam 2300 producing images at the magnification of 50 \times . The images were further binarized using a public domain image processing software ImageJ^[25] in order to discriminate between pores (black pixels) and the main structure (white pixels). Adjacent pores were differentiated using the “watershed” command. The porosity of each section was calculated as the ratio of black pixels in the total pixel count per image. The average pore size (d_p) was determined using **Eq. 2**:

$$d_p = 2\sqrt{\frac{A_p}{\pi}}, \quad (2)$$

where A_p is the average area of the actually observed pores (not necessarily circular).

Further, sample sections were analyzed using the electron microscope (Carl Zeiss Evo LS15 VP-Scanning Electron Microscope, SEM). In order to improve visualization of the non-conducting SiO_2 particles, a thin film of gold was sputter coated over the top surfaces. Additionally, chemical analysis of the sections was completed on un-sputtered samples employing the Energy-Dispersive X-ray Spectroscopy (INCA EDX system, Oxford Instruments).

The topological aspects of microstructure were examined by optical 3D surface metrology using InfiniteFocus® system (Alicona), which allows 3D reconstruction of a porous surface from vertical scans of small depth of focus optical beam in the visible range of spectrum.

In order to determine the mechanical response of the porous materials, all samples with sufficient handling strength were subject to uniaxial compression testing using a universal testing machine (INSTRON Model 4206, Norwood, MA). The tests were carried out at the deformation rate of $0.5 \text{ mm} \cdot \text{s}^{-1}$ and the obtained force-displacement data were transformed into stress and strain plots for analysis.

Finally, nanoindentation testing was carried out using the MTS Nanoindenter XP on polished axial and radial sections. The indentation points were selected over the sintered material; avoiding areas associated with pores. All measurements were carried out using a three-sided pyramidal Berkovich diamond indenter (end tip radius $\sim 200 \text{ nm}$) at a constant loading and unloading strain rate of 0.05 s^{-1} . The maximum surface penetration depth was of $2 \text{ } \mu\text{m}$ and the dynamic continuous stiffness measurement (CSM) method was used for fitting the indentation data. Prior to testing, the indenter was calibrated using an isotropic fused silica standard (elastic modulus of 72 GPa , indentation hardness 9 GPa). Young's modulus (E) of the tested sample was obtained by the method of Oliver and Pharr^[26] deriving its value after **Eq. 3**:

$$E = (1 - \nu_{316L}^2) \left(\frac{1}{E_{\text{red}}} - \frac{1 - \nu_{\text{ind}}^2}{E_{\text{ind}}} \right)^{-1}, \quad (3)$$

where ν_{316L} , E_{red} , ν_{ind} , and E_{ind} are the Poisson's ratio of steel ($\nu_{316L} = 0.3$), reduced Young's modulus, Poisson ratio of the diamond indenter ($\nu_{\text{ind}} = 0.07$), and Young's modulus of the indenter ($E_{\text{ind}} = 1141 \text{ GPa}$), respectively. The value of the reduced Young's modulus was determined using **Eq. 4**:

$$E_{\text{red}} = \frac{\sqrt{\pi}}{2\beta} \frac{S}{\sqrt{A_c}}, \quad (4)$$

where β , S and A_c are a geometry constant ($\beta = 1.034$ for the Berkovich tip), elastic contact stiffness and contact area established under load, respectively. The final value of Young's modulus was determined as an average of at least 15 individual indents determined from indentation depths ranging from 0.5 to 2 μm . The indentation hardness (H) was determined from the applied load (P) using **Eq. 5**:

$$H = \frac{P}{A_c}. \quad (5)$$

3. Results

3.1. Macro- and microstructure

The resulting porosity, apparent and real densities are summarized in **Table 1**. Not all of the samples could be characterized because they would not attain sufficient strength during either compaction or sintering. These samples would crumble when handled or manipulated, which made them difficult or impossible to handle. All the remaining samples resulted of higher porosity than that of the reference (R-0), which has a native porosity of 25 vol.% typical to this manufacturing process^{[16][22]}. Apparent densities of all the leached samples correspond with those deduced from cumulative mass loss (**Fig. 1**), whereas their bulk densities are in general lower than that of a molten and solidified 316L material (8.00 $\text{g}\cdot\text{cm}^{-3}$). Only the samples obtained by using the large space holder (L series) resulted in bulk densities similar to that of the reference sample (**Tab. 1**).

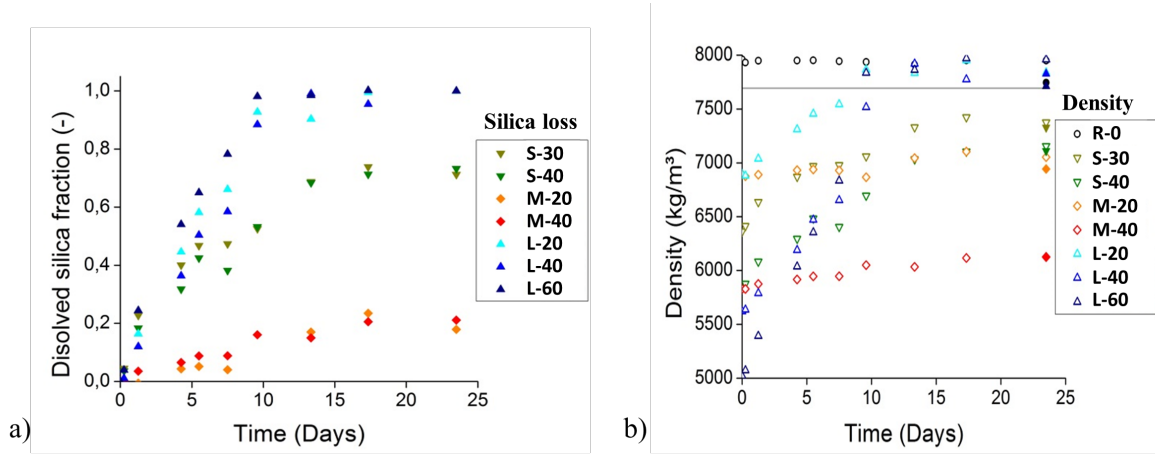


Fig. 1. Removal of silica by alkaline leaching of the compacted cylinders: a) cumulative silica loss as fraction of the initial content in time, (b) the same data presented in terms of real density in time.

Pore size and cumulative pore fraction obtained from the metallographic analysis are shown in **Fig. 2**. Whereas **Figs. 2a-d** are examples of original and processed images of selected samples, **Fig. 2e** summarizes all the results discriminating between radial and axial sections. In general, larger pore sizes are observed in radial sections as compared with their axial counterparts. It is also observed that about 50-80% of pores from the M series and about 50% of pores from the L series are larger than the space holder employed to produce them.

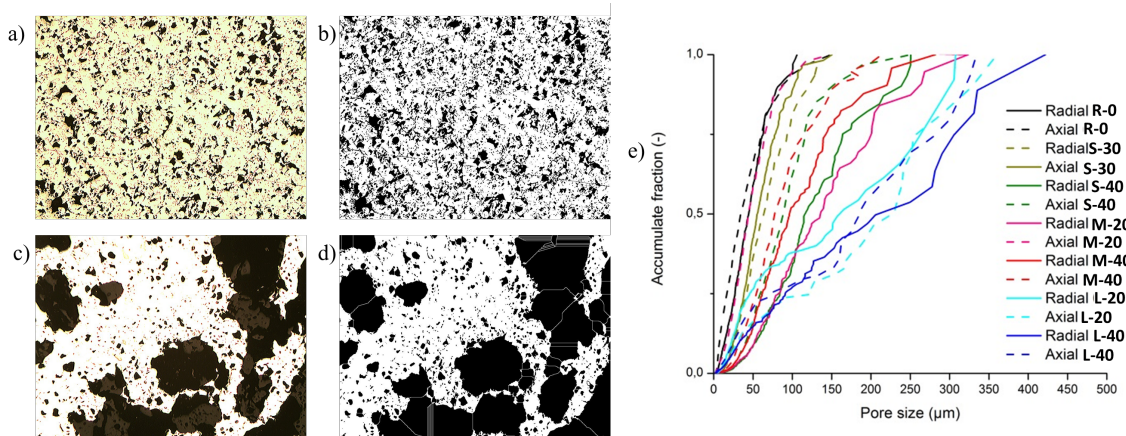


Fig. 2. Pore size analysis obtained by image processing: a) original optical micrograph of sample R-0, axial cut at 50×; b) processed image of a); c) original optical micrograph of sample L-20, axial cut at 50×; d) processed image of c); e) Cumulative pore fraction as a function of equivalent pore size.

The macro and microstructure observed by SEM in both axial and radial sections are shown in **Fig. 3**. In all the structures the shape of pores is irregular. The reference sample (R-0) shows the continuous metal matrix typical of a well-sintered metal. The number of pores observed in the radial section is visibly higher than its analogue in axial section. In all other samples a homogenous distribution of pores along and across the entire sample was observed; however with the same tendency of more pores present in the radial than axial sections. In addition, two types of pores could be discriminated: smaller ones associated with the sintering process and large ones associated with the removed silica spacer. This observation is especially pronounced in the L series. Further, the quality of sintering decreases with the increment of volume fraction of the space holder. The lower the quality of sintering the more likely is the damage in sample preparation to occur; for instance, rupture while polishing (see example in **Fig. 3**).

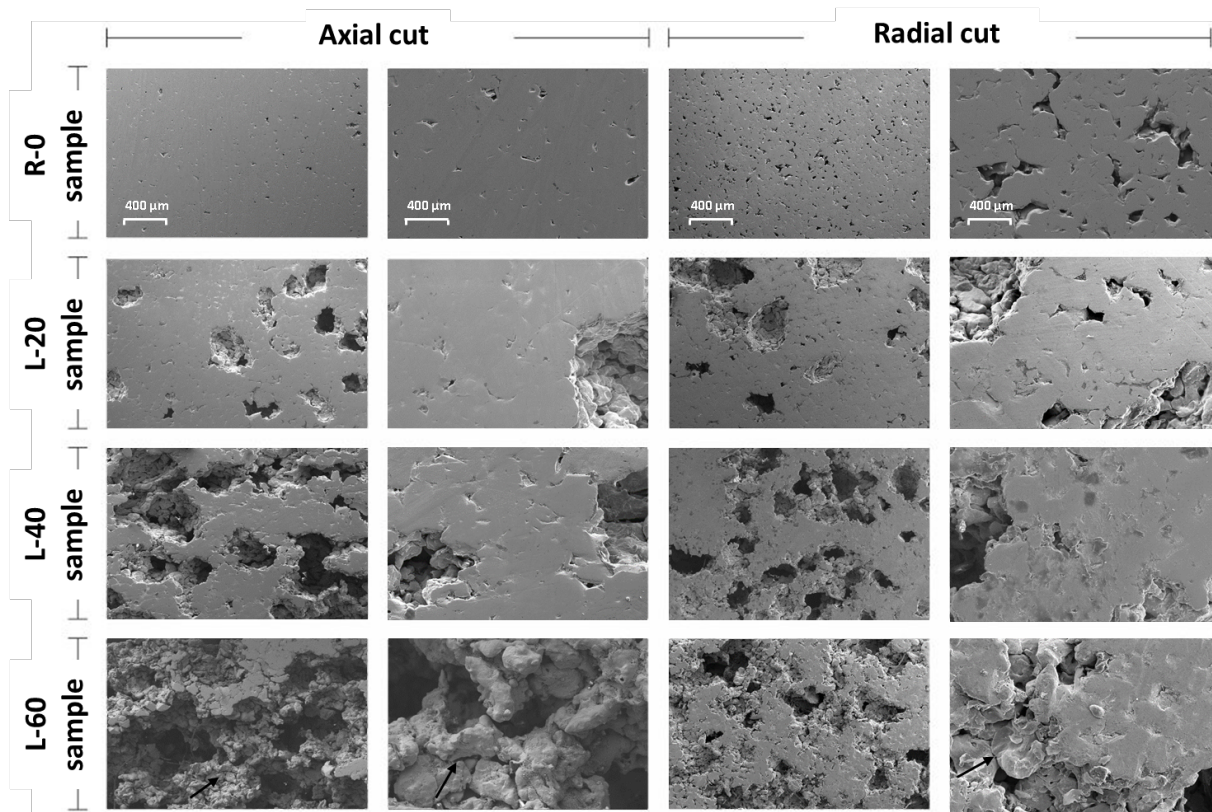


Fig. 3. Representative SEM micrographs of sintered and leached samples showing the macro- and microstructure of the axial and radial sections.

Results of the topological analysis of microstructure, showing more detail of the depth and sizes of pores, are presented **Fig. 4**. Negatively skewed surface parameters are obtained after

sample polishing on surface parameters analysis in the three samples analyzed. The surface profile shows a homogenous distribution of pores with low variation in depth and length size for sample R-0 (Fig. 4a). The distribution of porosity in samples L-20 and L-40 is also homogenous, however, with two types of pores: bigger ones associated with the removed silica and smaller ones associated with the sintering process. The height of the voids is indicated with color code in the 3D images shown in Figs. 4 a, 4 b and 4 c, where the dark blue corresponds with the maximum depth of valley in the analyzed profile. Again, the two types of pores are evidenced in the sample L-20 (Fig. 4d).

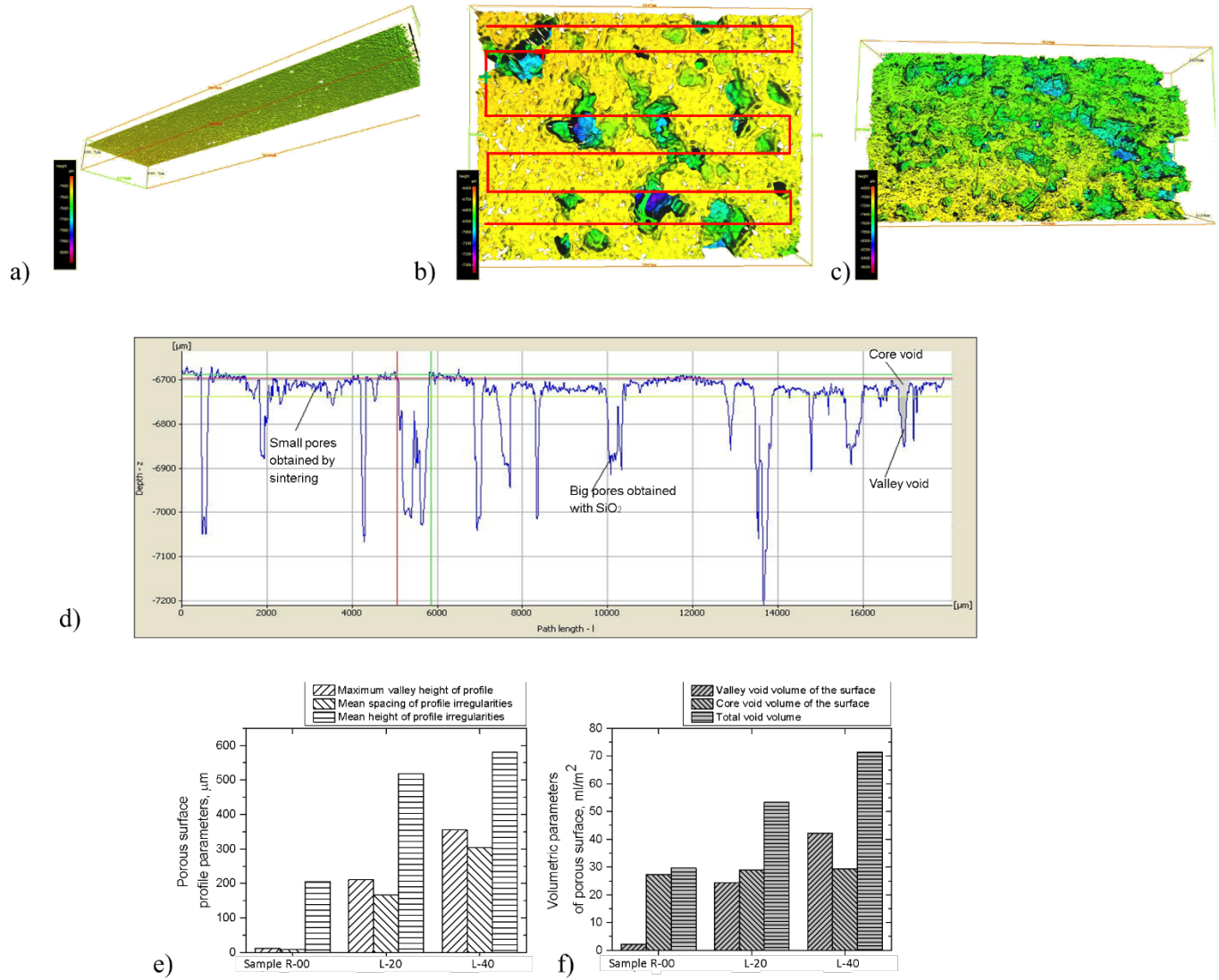


Fig. 4. Topographic analysis (Alicona) of the produced macrostructures: a) 3D model of sample R-0, b) sample L-20, and c) sample L-40; d) surface profile associated with the scan line indicated in b); Statistical data of all samples: e) profile parameters, and f) volumetric data.

The number and size of pores obtained by image analysis optical micrographs for both axial and radial cuts are consistent with the results obtained by Alicona analysis, which additionally provides information on the depth of the pores. The profile parameters (**Fig. 4e**) show that the increment of silica percentage is directly correlated with the increment of pore height, reflected in the maximum valley depth and valley void volume; parameters that are of low value for the reference sample. In the case of sample L-20, a higher volume of valley voids is detected than cores voids, which again corroborates the bimodal nature of its porosity. The mean spacing of profile irregularities, mean height of profile irregularities and total void volume (**Fig. 4f**) are further parameters directly correlated with the removal of SiO_2 , as an increment of all these values is observed for increasing percentage of silica removed.

No silica particles could be observed in the pores by inspection with optical microscope; however, EDX analysis under SEM reveals the presence of residual silica. It is especially the case in the S and M series as exemplified in **Fig. 5**.

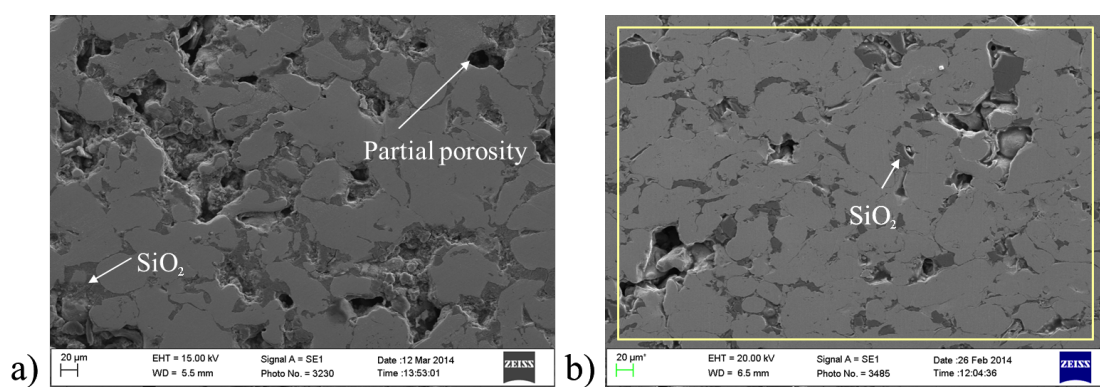


Fig. 5. SEM micrographs of silica particles entrapped in the sintered structures: a) sample S-30; b) sample M-20. The rectangle indicates the area used for chemical analysis (Tab. 3).

3.2 Mechanical properties

Compression test curves of the porous samples are shown in **Fig. 6** and the associated mechanical properties obtained from this data are listed in **Table 2**. The shape of all the stress-strain curves is typical of porous metal, showing an initial linear-elastic region until the compressive yield stress is reached. The values of elastic modulus range from 36 MPa for the most porous sample (L-60) to ~ 7.4 GPa for the reference sample (R-0), which is considerably lower than 190 GPa expected for a cast AISI 316L. The values of yield stress range from 4.2

MPa to 220 MPa, which are values that are similar to those reported in literature for steel with similar porosities^[14, 27-29]. Increasing porosity correlates with decreasing compressive strength and the plateau region becomes longer and with lower slope.

Table 2. Mechanical properties of selected samples.

Sample	E nanoind [GPa]	E compression [MPa]	Yield stress [MPa]	Densification strain [m·m ⁻¹]	Energy absorbed [MJ·m ⁻³]
Theoretical (cast)	190	190	200	-	-
R-0	155	7,370	165.0	0.220	63
L-20	85	962	108.0	0.630	115
L-40	62.5	201	17.4	0.545	10.9
L-60	32.5	36	3.8	0.660	3.3

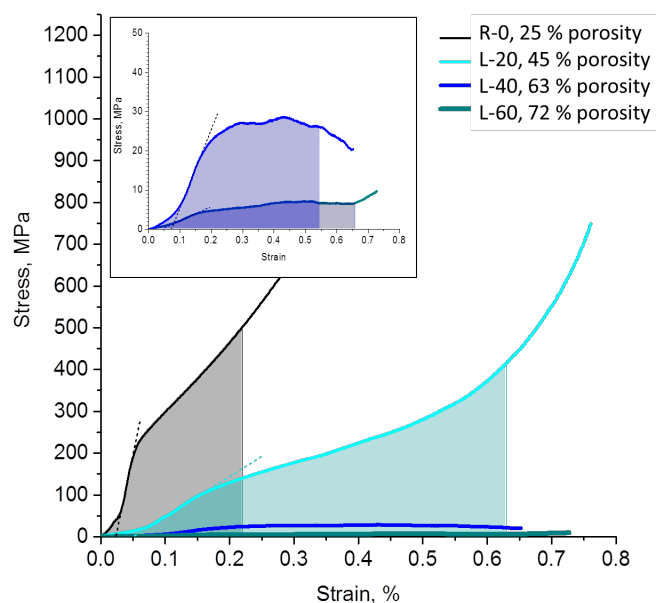


Fig. 6. Stress-strain curves of the porous samples under uniaxial compression.

The results of nanoindentation testing are shown in **Fig. 7**. The values of hardness and elastic modulus of all samples are lower than those of the reference and also lower from those expected for a cast alloy. The values of elastic modulus are systematically higher than those obtained from compression testing. An explanation is discussed in the following section.

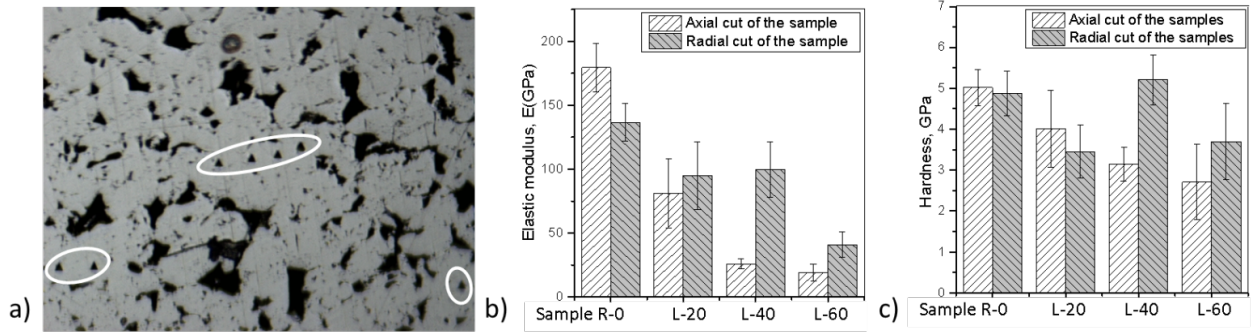


Fig. 7. a) Optical micrograph of porous sample R-0 showing residual indents on the metal surface; b) Elastic modulus and c) Hardness on porous AISI 316L samples, whose averaged values and standard deviations were derived from at least 15~20 individual indents.

4. Discussion

Stainless steel with interconnected porosity has been produced by the method of MPSH employing particles of silica as space holder. However, not all the samples could retain their mechanical integrity throughout the processing. This is especially true for samples of high content of the smallest silica sizes indicating that formation of necking is prevented due to incomplete compaction of the metallic particles. Producing high porosities of small pore size is therefore limited. The optimum processing conditions were obtained for the larger particles (200 μm); producing porosities between 45 and 72 vol.%. (samples L-20, L-40, L-60).

A native porosity of 25 vol.%, being a feature of the powder metallurgical processes, was obtained in the reference sample and might already represent some of the natural (biological) materials when pre-pressed or flaked ^[9]. However, the crucial aspect in physical modelling of the extraction from pre-pressed oilseeds is the interconnectivity between pores. This feature is assured by leaching the particles of space holder because the only way for the solubilized silica to be removed is by diffusion through the network of pores. Removal of all the silica would correspond with a perfectly interconnected network of pores; however it is not always achieved. Some of the particles remain fully trapped within the metallic matrix resulting in a bulk density lower than that of bulk steel. Because these entrapped particles are not exposed to the solvent they are indifferent to the extraction process; however, the fact poses a lower limit to the interconnected porosity that can be produced by the method.

The degree of interconnection between the silica particles determines tortuosity of the porosity and thus the time necessary to leach the space holder. In this study, only the largest particles (the L-series) could be removed completely within about two weeks (**Fig. 1**).

Leaching smaller particles would require longer leaching time. It should be noted that prolonging leaching time does not compromise integrity of the metallic matrix as shown by the reference sample, free of silica, which experienced no change of density when exposed to sodium hydroxide along with other samples for the entire duration of leaching (**Fig. 1b**). However, full removal might be prevented by the particle entrapment described above. The eventuality of retaining entrapped silica is suggested by saturation of the leaching curves at ca. 80% and 20% of initial silica content for the M- and S-series, respectively (**Fig. 1a**). This observation implies that the relation between initial silica content used for preparing the composite and final porosity of the product needs corrective to account for particle entrapment effects.

Corroborating these observations allows defining the optimum conditions for producing porous stainless steel pellets as those in which two perfectly interconnected networks are formed: one corresponding with the metallic particles which are sintered to form a continuum (the matrix); and one corresponding with silica particles which are removed to form open porosity.

The size of pores produced in the sintered steel is in general larger than that of nominal diameter of the space holder particles used to produce them. This might be attributed to the clustering of two or more silica particles during the mixing process as suggested in **Fig. 2d** where the application of watershed function in image processing allows detecting and visually separating some of these clusters.

Further, there is a difference in the size of pores in the radial and axial sections with the sizes in radial cut being systematically larger than those of their axial counterparts (**Fig. 2c**). This observation can be explained by the uniaxial compression of powder mixture prior to sintering step, which forces the particles to be displaced preferentially in the radial direction. Whereas metallic particles during compaction undergo displacement and possibly plastic deformation, ceramic particles are rearranged or crushed rather than deformed. The preferential flattening of metallic particles in the radial plane can be observed in **Fig. 3**. The difference in void size associated with radial and axial cuts is particularly notorious in the reference sample and supports the hypothesis of preferential clustering of ceramic particles in the larger radial voids.

Mechanical resistance of the porous pellets is important for the physical modelling of supercritical extraction. Disintegration of the pellet during the simulated process is not acceptable so that apart from the handling strength a minimum requirement of both elastic

modulus and yield strength will depend on the process specifications. Both of these quantities are determined by the quality of sintering, *i.e.* bonding between metallic particles that allows for homogenization of the metallic matrix that in the ideal case acquires the mechanical properties of its cast analogue. The last process is completed by recrystallization and grain growth during sintering, which produces necking of the metallic particles. The best quality of sintering was obtained in the reference sample as shown by the values of hardness and elastic modulus indicating that the presence of silica has a negative effect on sintering.

The decrease of mechanical properties with increase of porosity is observed for both axial and radial sections and correlates with the increment of initial silica content; however, radial cuts present higher values of hardness and elastic modulus as compared with their axial counterparts. The lowest values are obtained for the more porous samples (L-60), confirming weaker bonding between metal particles after sintering. This has also been observed under SEM.

The differences between the values of elastic modulus obtained from the two methods can be attributed to the scale at which this property is measured. Whereas the compression test involves the response of the entire (macroscopic) sample, including both the bulk and the pores, the nanoindentation test characterizes the more localized mechanical response which is predominated by the bulk 316L matrix. Nonetheless, it can be seen in **Fig.7** that nanoindentation data revealed a systematic drop of the effective stiffness behaviour as the pore content increases. As discussed before, knowledge of both properties are relevant for the overall mechanical performance of the pellet at different length scales.

Increased porosity correlates with decreased elastic modulus and decreased yield strength, although increased absorption of mechanical energy can be expected due to densification offset and higher strains for lower density structures.^[12] This last feature is relevant for the physical simulation of supercritical CO₂ extraction due to the mechanical conditions associated with the process.

5. Conclusions

Applicability of the metal powder space-holder (MPSH) technique for fabrication of model materials to study the process of supercritical CO₂ extraction has been demonstrated on the example of porous AISI 316L steel cylinders. By using SiO₂ as the space-holder and NaOH for its removal, it is possible to extend the variety of structures similar to those of natural

matrices that can be made of food grade stainless steel. The distinctive feature as compared with direct powder metallurgical approach is interconnectivity of the pores assured by leaching of the spacer. The pore size and volume fraction can be tuned by selecting particle size and volume fraction of the silica particles. However, this tuning has only been shown effective for porosities between 45 and 72 vol.% and for silica particles that are sufficiently interconnected as to allow their removal by leaching.

Received: ((will be filled in by the editorial staff))

Revised: ((will be filled in by the editorial staff))

Published online: ((will be filled in by the editorial staff))

References

- [1] J.M. del Valle, J.M. Aguilera, *Food Sci. Technol. Int.* **1999**, 5, 1.
- [2] NIST, Fluid Thermodynamic and Transport Properties, Version 5.0. (n.d.).
<http://www.nist.gov/srd/nist23.htm>.
- [3] J.M. del Valle, *J. Supercrit. Fluids* **2015**, 96, 180.
- [4] J.M. del Valle, J.C. de la Fuente, E.L. Uquiche, *J. Supercrit. Fluids* **2012**, 67, 60.
- [5] F.A. Urrego, G.A. Núñez, Y.D. Donaire, *J. Supercrit. Fluids* **2015**, 102, 80.
- [6] J.M. del Valle, J.C. de la Fuente, *Crit. Rev. Food Sci. Nutr.* **2006**, 46, 131.
- [7] E. Uquiche, J.M. del Valle, J. Ortiz, *J. Food Eng.* **2004**, 65, 55.
- [8] E. Uquiche, J.M. del Valle, M. Ihl, *J. Food Sci.* **2005**, 70, E379.
- [9] J.M. del Valle, J.C. Germain, E. Uquiche, C. Zetzl, & G. Brunner, *J. Supercrit. Fluids* **2006**, 37, 178.
- [10] F. Stüber, S. Julien, F. Recasens, *Chem. Eng. Sci.* **1997**, 52, 3527.

- [11] W. Clyne, I. O. Golosnoy, J. C. Tan, A. E. Markaki, *Phil. Trans. R. Soc. A-Math. Phys. Eng. Sci.* **2006**, 364 125.
- [12] J. Banhart, *Prog. Mater. Sci.* **2001**, 46, 559.
- [13] A.R. Kennedy, *Scr. Mater.* **2002**, 47, 763.
- [14] C. Tan, J. A. Elliott, T. W. Clyne, *Adv. Eng. Mater.* **2006**, 8, 495.
- [15] B.H. Smith, S. Szyniszewski, J.F. Hajjar, B.W. Schafer, S.R. Arwade, *J. Constr. Steel Res.* **2012**, 71, 1.
- [16] N. Kurgan, *Mater. Des.* **2014**, 55, 235.
- [17] Y.Y. Zhao, D.X. Sun, *Scr. Mater.* **2001**, 44, 105.
- [18] N. Bekoz, E. Oktay, *J. Mater. Process. Technol.* **2012**, 212, 2109.
- [19] I. Mutlu, E. Oktay, *Mater. Des.* **2013**, 44, 274.
- [20] H. Bakan, *Scr. Mater.* **2006**, 55, 203.
- [21] M.M. Dewidar, K. a Khalil, J.K. Lim, *Trans. Nonferrous Met. Soc. China (English Ed.)* **2007**, 17, 468.
- [22] C. Mapelli, D. Mombelli, a. Gruttadauria, S. Barella, E.M. Castrodeza, *J. Mater. Process. Technol.* **2013**, 213, 1846.
- [23] X. Zhou, S. Li, J. Li, Y. Liu, *J. Cent. South Univ. Technol.* **2008**, 15, 209.
- [24] J.T. Yao, J.Q. Ren, H.B. Huo, G.J. Yang, C.X. Li, C.J. Li, *J. Therm. Spr. Technol.* **2014**, 23, 991.
- [25] M.D. Abràmoff, P.J. Magalhães, S.J. Ram, *Biophotonics Int.* **2004**, 11, 36.
- [26] W.C. Oliver, G.M. Pharr, *J. Mater. Res.* **1992**, 7, 6.
- [27] A.C. Kayan, C. Fleck, *Mater. Sci. Eng.* **2014**, A 615, 447.
- [28] P.Quadbeck, K.Kümmel, R.Hauser, G.Standke, J.Adler, G.Stephani, B. Kieback, *Adv.Eng.Mater.* **2011**, 13, 11.
- [29] X. Lin, A. R. Kennedy, *Adv. Eng. Mater.* **2015**, 17, 6.